Highlights

Spatial Domain Mapping from In-Process Sensor Signals for Visual Inspection of Multi-Material Stack Drilling

Bin Chen, Chaoyue Niu, Erica Smith, Rob Bramley, Pete Crawforth, Mahdi Mahfouf, Visakan Kadirkamanathan

- Introduction of a novel *Spatial Domain Mapping* method by an in-process sensor signal integration framework to enable novel visualisation of the drilling process for the identification of anomalous patterns in the hole surface's quality in three-dimensional.
- Development of a variant model-based signal processing approach that exploits the sensor characteristics of the fibre optic sensor for both spindle speed and angle estimation, coupled with a feed rate estimator from the laser sensor.
- Assessment of the proposed *Spatial Domain Mapping* method on drilled holes from a manufacturing trial to demonstrate potential association between the in-process signal temporal profile and the spatial localisation of the hole machining process.

Spatial Domain Mapping from In-Process Sensor Signals for Visual Inspection of Multi-Material Stack Drilling

Bin Chen[a], Chaoyue Niu[a,*], Erica Smith[b], Rob Bramley[b], Pete Crawforth[b], Mahdi Mahfouf[a] and Visakan Kadirkamanathan[a]

[a]School of Electrical and Electronic Engineering, University of Sheffield, Sheffield, S10 2TN, U.K.
[b]Advanced Manufacturing Research Centre, University of Sheffield, Rotherham S60 5TZ, U.K.

ARTICLE INFO

Keywords:
Sensor Fusion
Industrial Monitoring
Manufacturing Informatics
Robotic Drilling
Composite Machining

ABSTRACT

Airliner assembly processes involve components being pre-assembled into a 'stack', which is then drilled through. Manufacturers have strict hole quality requirements and need confidence in hole quality, since defects such as burrs and delamination can affect structural integrity. Human expert can be empowered to perform hole quality inspection through the provision of useful information. Visual representations of signal features and their association to the spatial and temporal features in the hole quality is a powerful mechanism by which to facilitate quality inspection. This paper proposes a novel sensor signal integration framework to map sensor signals from the time domain to the relative spatial domain as indicated by the drill bit position. Kalman filter based rotational position estimation from fibre-optic signal and relative drilling depth estimation from laser signal provided the relevant spatio-temporal information for the mapping. The resulting spatial domain mapping enables visualisation of signals for the detection of any defect related anomalous patterns for a human expert to inspect the hole quality. Its potential is demonstrated on a real-world drilling trial of different quality holes.

1. Introduction

Drilling is a common machining process seen across a broad range of applications and industries. It is of particular significance in aerostructure assembly, where components are held together by fasteners, such as bolts and rivets, fitted through drilled holes. In fact, large commercial aircraft may have 1.5 to 3 million fasteners [1]. As defects in the holes reduce the structural integrity of joints, manufacturers normally have hole quality requirements. Burrs on metal (primarily aluminium and titanium) components [2], and delamination of fibre reinforced polymer (FRP) components [3], are both defects controlled by quality requirements. Given the high risk of the application, confidence in hole quality is essential.

Holes in mating components must align very well to accept tight fitting fasteners. To achieve this, holes are typically drilled while components are held together as a stack. However, before a fastener is fitted, components are typically disassembled to inspect for defects between layers and rectify them if necessary. This extra work is inefficient, slowing assembly speed and increasing production costs. Assembly without this intermediate disassembly is known as One-Way Assembly (OWA) [4].

With components held closely together, inspection between components using traditional techniques is highly challenging. One approach to gaining confidence in hole quality without intermediate disassembly is in-process monitoring using sensors. This involves recording, processing and analysing sensor signals to relate features of the signal to hole defects in a test environment, where components can be disassembled for inspection, and then applying the monitoring in production to identify defects through signal responses from drilling. Sensors such as load cells, accelerometers, and acoustic emission sensors are highly sensitive to physical responses and can be installed onto components, fixtures or drilling machines. Since data is gathered during the drilling process, process confidence could be improved without further steps in the assembly process being added. It has been shown that using in-process signals for early detection of defects, it can significantly reduce the risk of noncompliant products reaching later assembly stages or final inspection [5].

*Corresponding author
bin.chen@sheffield.ac.uk (B. Chen); c.niu@sheffield.ac.uk (C. Niu); erica.smith@amrc.co.uk (E. Smith); r.bramley@amrc.co.uk (R. Bramley); p.crawforth@amrc.co.uk (P. Crawforth); m.mahfouf@sheffield.ac.uk (M. Mahfouf); visakan@sheffield.ac.uk (V. Kadirkamanathan)
ORCID(s): 0000-0002-0397-5626 (B. Chen)

It is well established that high cutting forces lead to hole defects and there has been work relating in-process signals from drilling to hole defects [6]. For example, a physics-based fractal dimension analysis was used to process force signals to predict and improve hole quality (i.e., burr heights) in the metal layers of CFRP, Titanium (Ti), and Aluminium (Al) stacks [7]. Building on this relationship, force signals, such as those measured using integrated sensors in active-thrust spindles, have further demonstrated potential for enhancing process monitoring and control in robotic drilling [8]. A data segmentation method using axial force signals has been demonstrated to separate CFRP drilling, aluminum (Al) drilling, and countersinking stages in CFRP/Al stacks, thereby enabling more effective defect detection [9]. More recently, it has been shown that drilling force signals can be segmented—using peak and valley patterns—to identify critical transitions such as tool entry, material interface breakthrough, and burr formation [10].

Beyond force signals, other sensors have also been employed to monitor and control drilling processes. Vibration signals acquired from low-cost accelerometers have been used to extract features relevant to surface finish monitoring, demonstrating that effective process insights can be obtained even with minimal sensor setups [11]. Vision sensors, such as structured-light systems, have been utilized for 3D surface reconstruction and normal direction detection, which are critical for ensuring high-quality drilling outcomes [12]. Acoustic emission (AE) sensors, for example, have been used to identify defects during CFRP/Al stack drilling, with frequency analysis methods like fast Fourier transform enabling the classification of damage types [13].

Integrating and fusing multiple sensor data have been increasingly adopted for enhanced process monitoring and a number of machine learning methods have been proposed to support this trend. For instance, Bayesian fusion methods integrate diverse in-process signals (vibration and acoustic data), to improve drift detection and classification accuracy in ultra-precision machining [14]. Multi-sensor frameworks using accelerometers, acoustic emission sensors, and linear encoders have been employed to predict machining quality through Gaussian Process Regression models, effectively leveraging diverse sensor signals for robust prediction [15].

Beyond general monitoring, a related area of work focuses on adaptive hole-making in multi-material stacks by using either process-event recognition or tool-state estimation to modify cutting parameters. Pardo et al. characterised force, torque, AE and acceleration during stack drilling, demonstrating that these signals respond most distinctly to engagement, CFRP/Al interface transition, and exit, arguing that they can serve as reliable triggers for adjusting speed/feed (and even coolant supply) [16]. Zhang et al. cast stack drilling as incidence classification and achieved high accuracy using a support vector machine robust to wear; crucially, they explicitly position such recognition as an enabler for adaptive drilling, i.e., automatically adjusting cutting speed and feed when transitions or exit are detected [17]. In a different context, Denkena et al. develop a simulation- and data-driven assistance system that predicts shape error from tool engagement, and adapts the feed rate with the evolution of tool wear [18, 19].

While the above approaches focus on interpreting temporal process signals to classify an outcome, they typically do not provide spatial information about defect location. Traditional defect localization studies, such as those utilizing Lamb-wave imaging or triangulation, generally detect and visualize damage on stationary composite structures in an offline manner. These methods are not synchronized with tool movements, making them unsuitable for visualizing the dynamic drilling process or identifying precisely when and where along the hole defects form (a detailed comparison between these methods and our proposed approach is given in Table 1).

However, these are largely related to localization of accrued defects on a plate structure on two dimensions (2D) as opposed to defects due to drilling operations performed on them requiring 3D localization. Positional depth context is the missing link: the work [23] showed that integrating positional data can precisely identify bond locations when drilling Ti multi-alloys, however their study did not include circumferential resolution and multi-sensor signal integration. Hence, a strategy that combines real-time 3D spatial position with in process data to localize defects anywhere on the hole wall has yet to be reported.

To address the above limitations, a bespoke multisensor suite that collects synchronised signals for estimating the tool axial position and angular orientation was developed for drilling tests. Utilising these sensor signals, a signal processing framework can be created to estimate the tool position and orientation. Such an approach could be used to provide visualisation of information that is spatially and temporally localised, and thus give additional confidence in the evaluation of hole machining quality. Inspired by this idea, this paper develops a novel spatial domain mapping for visualisation with a sensor signal integration framework to support hole machining quality inspection from in-process data. The aim to provide such visual information to empower the human expert to make the quality inspection decisions. The main contributions are:

Table 1
Comparison of defect localization studies and this work

Aspect	**Yang et al. (2017) [20]**	**Liu et al. (2022) [21]**	**Zhou et al. (2023) [22]**	**This work**
Problem Domain	Lamb-wave non-destructive testing on stationary coupon; no drilling	Structural health monitoring of pre-damaged CFRP panel; no cutting involved	Delamination localization in damaged but fixed plate; no machining	Hole quality in drilling of multi-material stack with dynamic tool motion
Material and Structure	Woven glass fiber reinforced epoxy composite laminates; flat static plate	CFRP flat and stiffened plates with artificial delamination, holes, and cracks	Quasi-isotropic CFRP laminate; flat and stationary	Titanium–CFRP stack; dynamic drilling under machining conditions
Sensor Type and Deployment	Single type; Eight surface-mounted PZT (piezoelectric) sensors in non-circular array	Single type; SMART Layer embedded PZT network (dense transducer mesh)	Single type; Two "L" shaped PZT arrays (each with 7 sensors) surface-mounted	Multisensors: fiber optic sensor + AE sensor (on fixture) + laser displacement sensor
Application Deployment	Offline application for 2D plate defect monitoring	Online and offline application for 2D plate defect monitoring	Offline application for 2D plate defect monitoring	Online and offline application for in situ drilling 3D monitoring
Brief Overview of the Defect Localization Method	Lamb wave ellipse intersection, outputting 2D heatmap	Delay-and-Sum ultrasonic imaging to generate defect probability maps	Triangulation via time-difference-of-arrival; intersecting direction lines locate damage point	Time–space domain mapping: bursts in AE signal are projected to spatial positions along the drilled hole path

- Spatial Domain Mapping: Proposition of a novel method of spatial domain mapping based on sensor signal integration framework that synchronises the tool position and orientation with that of other in-process signals. This will allow visualisation of the drilling process stages and facilitate the identification of potential relationships between anomalous patterns in the sensor data and the quality of the hole surface in 3D.
- Signal Processing to Estimate Tool Axial and Angular Position: Design of a variant model-based signal processing method for a fibre optic sensor based on sensor characterisation for spindle speed and angle estimation, coupled with a feed rate estimator from the laser sensor. Both information extracted from the sensors are important control parameters for the drilling process and can be estimated in real-time from the in-process signals.
- Assessment of the Spatial Domain Mapping: Assessment of the proposed spatial domain mapping method to indicate its usefulness by an analysis on drilled holes from a manufacturing trial. Its role is in showing a qualitative association between spatially resolved patterns of AE signals and potential defects with the promise that the spatial domain mapping can become a platform for hole quality defect localization.

The rest of this article is summarised as follows: Section 2 describes the machining platform and discusses the problem; Section 3 proposes a model based formulation for the estimation of feed rate and depth of the tool from the laser displacement sensor; Section 4 considers the estimation for relative angle and rotation speed of the spindle, by using a novel signal processing method that takes sensor characteristics into account; Section 5 proposes a sensor signal integration framework to map in-process sensor data spatially and correlates features of this pattern with the hole quality from two cases; Section 6 concludes the paper and identifies future research.

Remark 1. *Some preliminary results on the signal processing for the fibre optic sensor have been reported in our conference paper [24]. This article develops a sensor signal integration strategy that combines the signal processing method on fibre optic sensor with a signal processing method for the laser distance sensor to support the sensor signal integration framework for spatial domain mapping in the OWA research.*

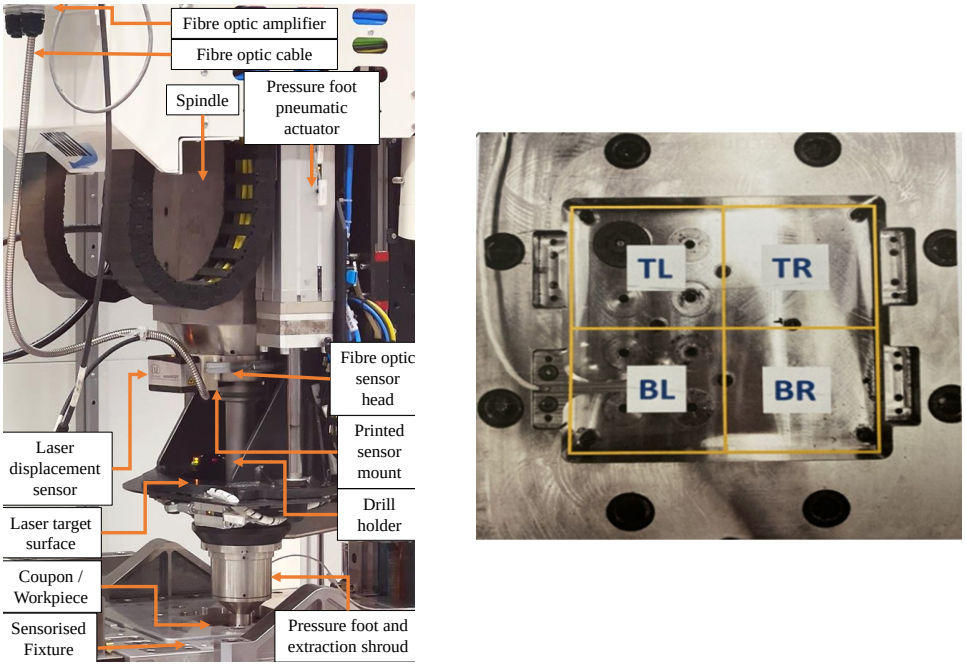

(a) Drilling platform and fixture.

(b) Example workpiece mounted in the fixture.

Figure 1: Equipment set-up of the machining platform.

2. Problem formulation

The drilling platform is first described in order to provide context to the formulation of the problem.

2.1. Metal-composite stack machining platform

The drilling platform, an example workpiece, and the fixture used in the case study are pictured in Figure 1. The drilling platform (in Figure 1a) is a Loxin T9000 parallel kinematic machine (PKM). PKMs offer a compromise between highly adaptable serial arm robots, and machine tools that are designed for high stiffness and accuracy. It is equipped with a specialized end effector including a pressure foot for enhanced stability, and a spindle mounted on a quill axis.

The workpiece is clamped along all edges and the fixture is mounted on a robust metallic base, shown in Figure 1b. The figure, fixture, and workpiece have their top right, top left, bottom right, and bottom left corners labelled with TR, TL, BR, and BL identifiers, respectively. These marks function as alignment points, offering a reference for orientation that facilitates the placement and guidance of the drilling process.

The spindle is an IBAG HT 210.3 A 24 CHIKPSVW (including an integrated encoder), and the machining process is regulated by the Siemens SINUMERIK 840D numerical control system. When commencing the machining test, the controller will activate the PKM, position the end effector, and follow the control parameters (e.g., the feed rate, drilling depth, and spindle speed) to execute the drilling process. Sensors within the manufacturing cell capture in-process data as part of the process monitoring system, allowing subsequent analysis to assess the machining quality.

The drilling procedure was performed on a multi-layer stack, indicative of typical structural arrangements in aeroplane assembly. CFRP is commonly used in aerospace applications owing to its superior specific stiffness, strength, and exceptional fatigue resistance [25]. However, its diminished interlaminar strength and inadequate impact resistance often lead to compromised joints at mechanically fastened sites [26]. To address this issue, CFRP is often combined with metallic alloys to form hybrid stacks, and this combination of materials improves the structure's performance more than either material could do on its own by using their different strengths [27].

Consequently, the workpiece in this study is designed to follow such a hybrid configuration. It is a stack made up of layers, with CFRP at the bottom and Ti at the top. Layers are separated by a thin gap filled with a wet replica sealant, representative of sealants used in airframes. The 0.15 mm gap was deliberately introduced to simulate typical

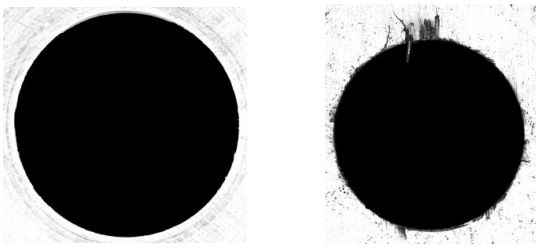

(a) Hole entry. (b) Hole exit.

Figure 2: Inspection image of example hole's quality.

assembly conditions in aerospace applications, where thin sealant-filled gaps are commonly present between joined components. Note that these two layers' materials have different properties, and hence the control settings are adjusted for each layer to account for these differences.

2.2. Spatial domain mapping visualisation case study

The case study for the spatial domain mapping based visualisation involves robotic hole drilling of a stack formed by a composite and a metal. In our experimental trial, a total of nine holes were drilled and their quality was assessed through post-drilling inspections. These holes were all machined using the same stack configuration, drill bit and control commands as detailed in Table 2 and Table 3, respectively. Note that the drill bit parameters are important for the later visualisation and analysis of the drilling process: the cutting diameter defines the hole geometry in 3D visualisation, and the point height is used to locate the breakthrough distance in the spatial mapping.

Table 2
Key parameters of the example stack and the drill bit.

Thickness of Ti layer	Thickness of gap	Thickness of CFRP layer	Cutter diameter of drill	Point height of drill
10.01mm	0.15mm	10mm	6.35mm	2.85mm

Table 3
The control commands for the drilling process

Spindle speed for Ti layer	Feed rate for Ti layer	Spindle speed for CFRP layer	Feed rate for CFRP layer
4010.20 RPM	481.22mm/min	5764.67 RPM	345.88 mm/min

From these drilled holes, the hole exhibiting the most pronounced defect (characterized by an obvious crack at the hole exit) and the associated in-process and part data, are used to illustrate the framework development. Please refer to Section 4 in the Supplementary Material for the results of spatial domain mapping applied to all the holes from the trial. Figure 2 shows the post-drilling inspection of this exemplified hole's entry and exit quality. For the example stack, CFRP delamination and uncut fibres can be seen at the hole exit.

For all sensors used in the experiment, we list their types and mounting layout in Section 1 of the Supplementary Material. These sensors were installed both on the workpiece and on the spindle. For the workpiece-mounted configuration, four Kistler load cells were positioned at the corners of the clamping frame to record cutting forces, and four accelerometers were fixed beneath the plate to capture vibration. Acoustic emission (AE) sensing was performed using four Mistras AE sensors arranged around the plate: during each hole drilling, the sensor positioned closest to the drilling site was activated to maintain a consistent sensing distance. An additional AE sensor was mounted on top of the workpiece and could be repositioned between holes to capture signals from different locations. Please refer to Section 1 of the Supplementary Material for the full diagrams.

For the spindle-mounted configuration (see Figure 1a in the Supplementary Material for placement), a laser displacement sensor (Micro-Epsilon ILD1900, 25.6 kHz) was fixed in the Z-axis direction relative to the drill to track

axial feed motion, and a fibre-optic sensor (Omron E3NX-FA41, 51.2 kHz) was mounted to measure rotational position. These two spindle sensors require additional signal processing steps to extract useful quantities such as feed rate and spindle speed. In the following sections, we describe the signal processing methods designed for both sensors.

3. Processing for laser displacement signal

Computation of feed rate from the laser displacement sensor can be carried out by differencing the signal. However, this can amplify the noise and small variations that lead to inaccurate estimates. A model-based approach that avoids noise amplification is the use of a constant velocity model [28], followed by estimation using the Kalman Filter [29].

3.1. Model based estimation for feed rate

In model-based signal processing, a signal model is postulated that relates the quantities of interest to the measurements.

The discrete-time constant velocity model is given by:

$$\begin{aligned} \begin{pmatrix} d(k+1) \\ v(k+1) \end{pmatrix} &= \begin{pmatrix} 1 & -T_s \\ 0 & 1 \end{pmatrix} \begin{pmatrix} d(k) \\ v(k) \end{pmatrix} + \begin{pmatrix} T_s \\ 1 \end{pmatrix} \varpi_l(k) \\ y_l(k) &= \begin{pmatrix} 1 & 0 \end{pmatrix} \begin{pmatrix} d(k) \\ v(k) \end{pmatrix} + \epsilon(k) \end{aligned} \tag{1}$$

where k is the discrete time index; T_s is the sampling time; $d(k)$, $v(k)$ and $y(k)$ are the true displacement, feed rate and the measured displacement at discrete time k; $\varpi_l(k)$, $\epsilon(k)$ are the uncorrelated zero mean white noise disturbance and measurement noise with variances $\boldsymbol{Q}_l$ and $\boldsymbol{R}_l$ respectively. Note that the drilling direction is downward so that displacement decreases with positive velocity as reflected in the model.

Then, we can further simplify the above model into a linear state space model as follows:

$$\begin{aligned} x_l(k+1) &= F_l x_l(k) + G_l \varpi_l(k) \\ y_l(k) &= H_l x_l(k) + \epsilon(k) \end{aligned} \tag{2}$$

where $x_l(k) = (d(k) \;\; v(k))^\top$, $H_l = (1 \;\; 0)$, and F_l as:

$$F_l = \begin{pmatrix} 0 & -T_s \\ 0 & 1 \end{pmatrix}, \quad G_l = \begin{pmatrix} T_s \\ 1 \end{pmatrix} \tag{3}$$

Now, we have the model-based estimation for the laser displacement sensor and the standard Kalman Filter (refer to [29] for more details) can be applied to get the system state estimates $\hat{x}_l(k)$.

Remark 2. *Note that, the choice of measurement noise variance $\boldsymbol{R}_l$, and process variance $\boldsymbol{Q}_l$ are important for the filtering operation of the Kalman Filter. Estimation of $\boldsymbol{R}_l$ can be obtained by observing the non-machining part and as it is sensor specific in the same environment, we only need to calculate it once. $\boldsymbol{Q}_l$ is normally chosen based on the variation of the speed, which in this case was chosen to have the same value as the measurement variance.*

3.2. Filtering results

The constant velocity model based Kalman filtered displacement estimate $\hat{d}(k) = (1 \quad 0)\,\hat{x}_l(k)$ is shown in Figure 3a. It demonstrates that the filtering result can reduce the noise effect on the original data and return an accurate estimation of the real-time height on the z-axis. Similarly, the feed rate is calculated by $\hat{v}_l(k) = (0 \quad 1)\,\hat{x}_l(k)$ (further multiplied by 60 to convert the result from mm/sec into mm/min) with Figure 3b showing the filtered estimate of the feed rate from the Ti layer to the CFRP layer. The figure shows the resulting feed rate fluctuating around the control command values as given in Table 3. This verifies the effectiveness of the proposed signal processing method to remove the effects of laser sensor noise.

Remark 3. *In addition to the qualitative assessment, the Kalman filter covariance provides a quantitative measure of uncertainty for the displacement state. The diagonal entry corresponding to the axial position converged to a steady-state variance of 4.6×10^{-6} mm^2, which corresponds to a 1σ standard deviation of 0.0021 mm. This indicates that the filtered displacement estimates are reliable to within a few micrometres of uncertainty.*

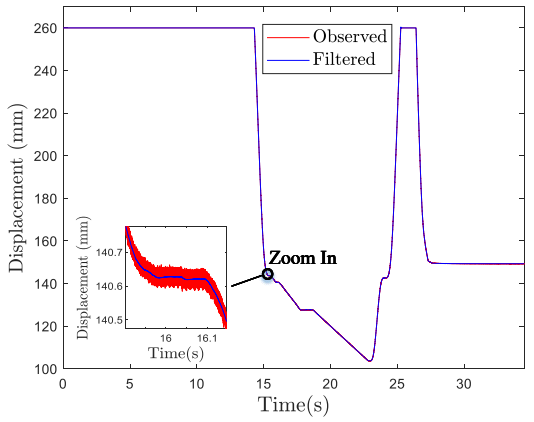

(a) The observed displacement from the sensor and the filtered displacement.

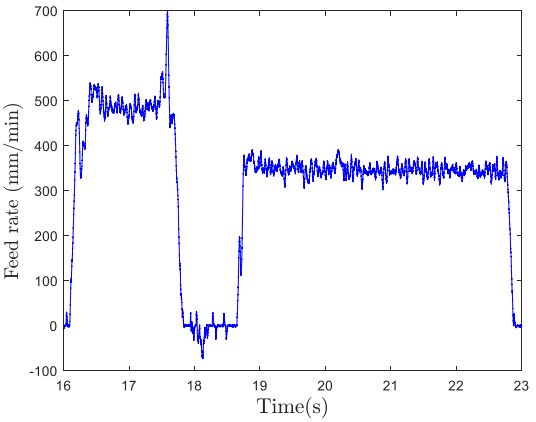

(b) The filtered feed rate when machining the Ti-CFRP stack.

Figure 3: The filtered displacement and feed rate from laser displacement data.

4. Signal processing for fibre optic sensor

The signal processing framework for the fibre optic sensor requires a more complex set of operations than that for the laser displacement sensor. We will adopt a model-based strategy as for the laser sensor, but with several stages to account for the fibre optic sensor characteristics. In the following section, we will model the transient response characteristics of the sensor to obtain its ideal response, thus eliminating transient effects.

4.1. Signal transformation and sensor characterisation

The fibre optic sensor signal illustrated in Figure 4a shows that it has a saturation amplitude when a light patch is sensed and a varying envelope when the dark patch is sensed. Note that, there exists one 'double-notch' pattern every 360 degrees (after every eight 'single-notch' patterns), which is used to represent the reference angle. Furthermore, the zoomed in signal shows that there are also transients that make it difficult to detect sensor transitions from seeing light and dark patches.

A two stage operation is first performed to transform the observed signal. We first perform a DC and sign shift to transform its raw data into a signal that has the following behaviours at time t: 0 output as the strip's light patch is traversed through by the fibre optic sensor and some non-zero signal level if the sensor passes through the dark patch. Then, by defining the raw observed sensor data as $z(t)$, we can obtain the transformed data $\tilde{z}(t)$ as follows:

$$\tilde{z}(t) = z^* - z(t) \tag{4}$$

in which z^* denotes the saturated DC voltage level of the sensor output upon receiving light intensity above some threshold, a sensor characteristic that is known a priori. Note that the envelope of the transformed signal $\tilde{z}(t)$ has varying output levels, which is indicative of the signal not reaching the maximum values z^*, attributed to slow transient characteristics. This phenomenon is inherent to the fibre optic sensor, and hence the characterisation of the sensor to ascertain its transient time constant can be conducted offline. This characterization would be useful for further signal-processing steps.

The second step is to view the transient signal as a dynamic response to some unobserved encoder type signal. We model this explicitly as a step response behaviour of generating a transient output $g(t)$ to an ideal step input signal $h(t)$. This response is indicative of the sensor's response to the rotating dark-light strip and can be denoted by a first-order linear system transfer function $G(s) = \alpha/(s + \alpha)$, where α represents the inverse time constant. It follows that,

$$g(t) = \alpha \int_0^t e^{-\alpha(t-\tau)} h(\tau) d\tau \tag{5}$$

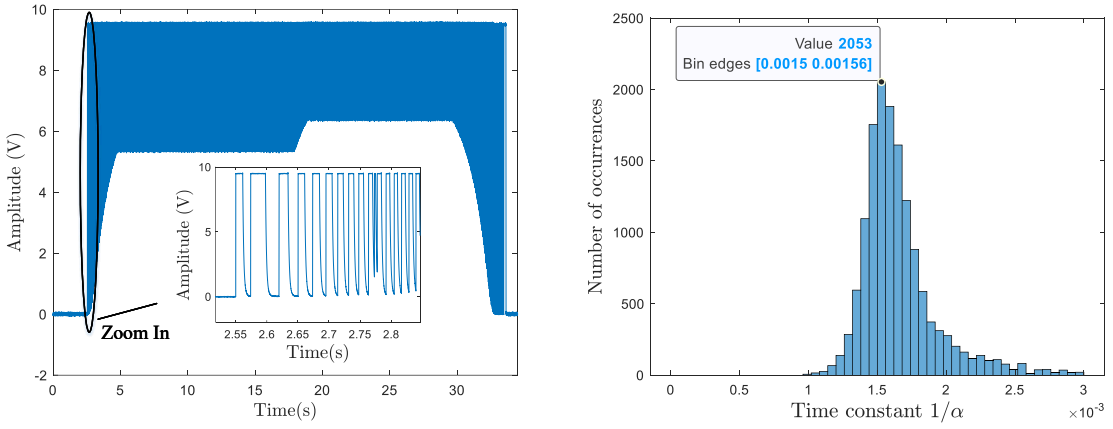

(a) Data from the fibre optic sensor.

(b) The distribution of time constant $1/\alpha$.

Figure 4: Raw data and characterisation of fibre optic sensor.

in which the ideal step input signal $h(\tau)$ is denoted as

$$h(\tau) = \begin{cases} 0 & \text{if } \tau < 0 \\ a & \text{otherwise} \end{cases} \tag{6}$$

and the maximum amplitude a is known *a priori*, set to 9.5.

Note that Equation (5) has a closed-form solution as follows,

$$g(t) = a(1 - e^{-\alpha t}). \tag{7}$$

Noting the fact that,

$$(1 - e^{-2\alpha t_0})/(1 - e^{-\alpha t_0}) = 1 + e^{-\alpha t_0}, \tag{8}$$

and then if we choose $t_2 = 2t_1 = 2t_0$ and record the output $g(t_0)$ and $g(2t_0)$, the inverse time constant α can be estimated without knowing the exact value of a. Considering,

$$g(2t_0)/g(t_0) = 1 + e^{-\alpha t_0}, \tag{9}$$

which can be rewritten as,

$$\alpha = \frac{1}{t_0} \ln \left\{ \frac{1}{\frac{g(2t_0)}{g(t_0)} - 1} \right\} = \frac{1}{t_0} \ln \left\{ \frac{g(t_0)}{g(2t_0) - g(t_0)} \right\}. \tag{10}$$

The above process presents a methodology for estimating the parameter α characterising the sensor. This estimation relies on the ability to accurately identify the initial time point $t = 0$ of the transient signals following the transformation. However, this is challenging and will incur a degree of variability to its identification and thus to the estimation of the parameter α. Given the many transients in the signal, a mitigation way to reduce the effect of this uncertainty is to choose a variety of such measurements and construct a histogram from which to derive the optimal estimate for α. This will reduce any induced noise in the parameter value from the uncertainties.

In summary, we can characterise the sensor behaviour and estimate the time constant using the following steps:

Step 1. On each rising period i of the signal $\tilde{z}(t)$, identify the local reference point of $t = t_i$ at which point the signal starts rising, corresponding to the local time $t' = 0$;

Step 2. Choose t_0 and collect signals $g_i(t' = t_0) = \tilde{z}(t = t_i + t_0)$ and $g_i(t' = 2t_0) = \tilde{z}(t = t_i + 2t_0)$;

Step 3. Use Equation (10) to calculate α_i using $g_i(t' = t_0)$, $g_i(t' = 2t_0)$ and t_0 for several i;

Step 4. Construct the histogram of $1/\alpha_i$ for all i and choose the mode of the distribution as the optimal time constant estimate $1/\hat{\alpha}$.

Applying the above procedure to the fibre optic sensor installed on the spindle results in the histogram for the parameter values for $1/\alpha$ shown in Figure 4b. The histogram exhibits a sharply defined peak, indicating a unique mode. Therefore, the optimal estimate can be efficiently determined and the estimated time constant is $1/\hat{\alpha} = 0.00153$ for the sensor used in the experiments. It should be noted that this is a specific characteristic of a fibre optic sensor, and hence it only needs to be determined once from a preliminary experiment.

4.2. Signal decomposition and measurement model

The fibre optic sensor signal processing is needed for the estimation of both the spindle speed and angle. It requires the outcome of the signal transformation to capture both the encoder-type rotational data and data pertinent to the 0° angle of the tool position. Having transformed the raw observed signal and characterised the transients of the sensor signal, a model based approach can be adopted to estimate the quantities of interest. In the following, we introduce a signal decomposition method (using hypothesis testing [30]) to extract these two types of information.

We consider the transformed discrete-time data $\tilde{z}(k)$ as the sensor filtered signal being driven by an ideal signal $u(k)$ that represents a pulse like signal of 0 amplitude when the sensor sees a light patch and an amplitude of 1 as it sees a dark patch. Given that the sensor either sees a light or a dark patch at any given time, we consider the decision problem of whether the ideal input is 0 or 1 as a hypothesis based detection problem:

$$u(k) = \begin{cases} 1 & \text{when } H_1 \text{ is true} \\ 0 & \text{when } H_0 \text{ is true} \end{cases} \tag{11}$$

where the hypothesis H_0 represents instances when the fibre optic sensor sees the light patch on the strip and the alternative hypothesis H_1 represents instances when the sensor sees the dark patch at time instant k. Under the transfer function sensor characterisation, the transformed signal can be expressed as:

$$\tilde{z}(k) = (1 - \alpha T_s)\tilde{z}(k-1) + (\alpha T_s a)u(k) + \zeta(k) \tag{12}$$

where a is the maximum sensor voltage amplitude as defined previously and $\zeta(k)$ is a zero mean noise component that captures the variations in the transformed signal. Given the linearity of the above model and with assumptions of Gaussianity for $\zeta(k)$, the estimation problem of $u(k)$ reduces to the detection problem which can be solved by using the likelihood ratio test [30], with the test further reduced as given below:

$$\hat{u}(k) = \begin{cases} 1 & \text{if } \frac{[\tilde{z}(k) - \hat{\tilde{z}}_{H_0}(k)]^2}{[\tilde{z}(k) - \hat{\tilde{z}}_{H_1}(k)]^2} \geq 1 \\ 0 & \text{otherwise} \end{cases} . \tag{13}$$

where $\hat{\tilde{z}}_{H_0}(k)$ is the predicted output if at time instant k, the hypothesis H_0 is true and $\hat{\tilde{z}}_{H_1}(k)$ is the predicted output if at time instant k, the hypothesis H_1 is true. These predicted terms based on the model description are given by,

$$\begin{aligned} \hat{\tilde{z}}_{H_0}(k) &= (1 - \alpha T_s)\tilde{z}(k-1) \\ \hat{\tilde{z}}_{H_1}(k) &= (1 - \alpha T_s)\tilde{z}(k-1) + \alpha T_s a \end{aligned} \tag{14}$$

where a is the maximum sensor voltage amplitude as defined previously. Applying the above hypothesis testing procedure results in the signal $\hat{u}(k)$ shown in Figure 5a.

The estimated signal $\hat{u}(k)$ is a series of pulses that detect changes in the signal $\tilde{z}$. However, the signal $\hat{u}(k)$ still contains the double-notch effects, making it difficult to estimate the spindle speed and angle. To address this problem, a further signal decomposition is developed to detect the notch signal associated with 0°, and another signal that removes the effect of the double notch but detects the regular dark /light patch transitions, as shown in Algorithm 1. It results in signals $\hat{u}_1(k)$ and $\hat{u}_2(k)$ (as shown in Figures 5b and 5c, respectively):

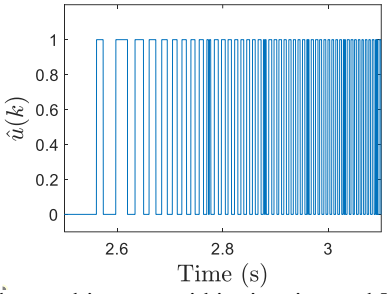

(a) The resulting $\hat{u}(k)$ within time interval [2.5,3.1].

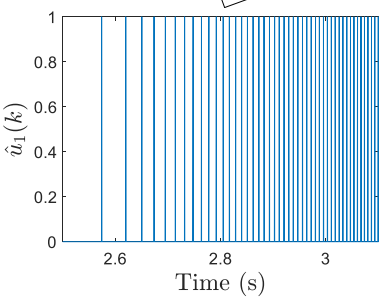

(b) The impulse input $\hat{u}_1(k)$.

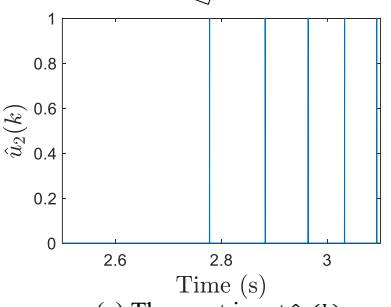

(c) The reset input $\hat{u}_2(k)$.

Figure 5: Extracted signals $\hat{u}(k)$, $\hat{u}_1(k)$ and $\hat{u}_2(k)$.

- Impulse input $\hat{u}_1(k)$:

$$\hat{u}_1(k) = \begin{cases} 1 & \text{if spindle has rotated by } \Delta_\theta \\ 0 & \text{otherwise} \end{cases} \tag{15}$$

- Reset input $\hat{u}_2(k)$:

$$\hat{u}_2(k) = \begin{cases} 1 & \text{if a double notch is detected} \\ 0 & \text{otherwise} \end{cases} \tag{16}$$

in which $\Delta_\theta = 40°$ represents each dark/light sector's angle range. Using $\hat{u}_1(k)$ and $\hat{u}_2(k)$, a pseudo-measurement signal for the angle θ can be created as follows:

$$y(k) = \begin{cases} 0 & \text{if } \hat{u}_1(k) = 1 \ \& \ \hat{u}_2(k) = 1 \\ y(k-1) + \Delta_\theta & \text{if } \hat{u}_1(k) = 1 \ \& \ \hat{u}_2(k) \neq 1 \\ y(k-1) & \text{otherwise} \end{cases} \tag{17}$$

with $y(0) = 0$. The signal $y(k)$ has a step-wise pattern with steps at the falling changes and resets to 0 for every revolution. Note that, this signal is not a direct measurement of the true angle but it conforms with the true angle value whenever $\hat{u}_1(k) = 1$ if the effect of any noise has been mitigated.

4.3. Signal model and model based estimation

The previous subsection provided estimates of signals $\hat{u}_1(k)$ and $\hat{u}_2(k)$, with one consisting of pulses for every Δ_θ increments and the other consisting of pulses for every complete revolution. This subsection is devoted to extracting an estimate for the spindle angle $\theta(k)$, relative to a reference position of 0° and the spindle speed $\omega(k)$ at k. Allowing for variations in these quantities over time that is induced by varying but unmeasured torque, once again, a model based

Algorithm 1. *Real-time decomposition for signal* $\hat{u}(k)$

Initialization: $\tilde{u}(0) = \hat{u}_1(0) = \hat{u}_2(0) = T = c = 0$
For: $k \geq 1$
  $\tilde{u}(k) = \tilde{u}(k-1) + \hat{u}(k)$
  If: $\hat{u}(k-1) = 1$ && $\hat{u}(k) = 0$
    If: $c = 1$
      $\hat{u}_2(k) = 1;\ c = 0$
    End If
    If: $\tilde{u}(k) \leq 0.5T$ && $c = 0$
      $\tilde{u}(k) = 0.5T;\ c = 1$
    Else:
      $T = \tilde{u}(k-1);\ \hat{u}_1(k) = 1;\ \tilde{u}(k) = 0$
    End If
  Else:
    $\hat{u}_1(k) = 0;\ \hat{u}_2(k) = 0$
  End If
End for
Return: Impulse input $\hat{u}_1(k)$ and reset input $\hat{u}_2(k)$

representation can be deployed with the change in angular acceleration $\varepsilon(t)$ as an unknown disturbance being a proxy for the changes in torque.

Denoting the spindle angle (in relation to the reference position of 0°) as $\theta(t)$, the spindle speed and angular acceleration can be defined as $\omega(t) = \dot{\theta}(t)$ and $\eta(t) = \dot{\omega}(t)$. Using the *constant acceleration model* [28] gives the following representation for the spindle dynamics:

$$\begin{pmatrix} \dot{\theta}(t) \\ \dot{\omega}(t) \\ \dot{\eta}(t) \end{pmatrix} = \begin{pmatrix} 0 & 1 & 0 \\ 0 & 0 & 1 \\ 0 & 0 & 0 \end{pmatrix} \begin{pmatrix} \theta(t) \\ \omega(t) \\ \eta(t) \end{pmatrix} + \begin{pmatrix} 0 \\ 0 \\ 1 \end{pmatrix} \tilde{\varepsilon}(t) \tag{18}$$

where the unknown disturbance is $\tilde{\varepsilon}(t)$. Its discrete-time form (with sampling time denoted as T_s) is represented as:

$$x_f(k) = F x_f(k-1) + G\varepsilon(k) \tag{19}$$

where $x_f(k) = (\theta(k)\ \ \omega(k)\ \ \eta(k))^\top$ is system state at instant k, $\epsilon(k)$ is assumed zero mean with variance Q_f,

$$F = \begin{pmatrix} 1 & T_s & \frac{1}{2}T_s^2 \\ 0 & 1 & T_s \\ 0 & 0 & 1 \end{pmatrix}, \quad G = \begin{pmatrix} \frac{1}{2}T_s^2 \\ T_s \\ 1 \end{pmatrix}. \tag{20}$$

Given a state-space model to denote the spindle's dynamics, the next step is to link the states to the observed data through a measurement equation. With the transformed sensor output $y(k)$ being a step-wise signal, an additional variable $\tilde{\theta}(k)$ is defined that maps to the signal $y(k)$ whilst also relating to the true angle $\theta(k)$. This leads to the measurement equation:

$$y(k) = \tilde{H}\tilde{x}_f(k) + \nu(k) \tag{21}$$

where $\tilde{x}_f(k) = \left(\tilde{\theta}(k)\ \ \theta(k)\ \ \omega(k)\ \ \eta(k)\right)^\top$ is the augmented state, $\nu(k)$ is induced noise due to signal transformations into $y(k)$ assumed zero mean with variance R, and

$$\tilde{H} = \begin{pmatrix} 1 & 0 & 0 & 0 \end{pmatrix}. \tag{22}$$

The auxiliary variable $\tilde{\theta}(k)$ is given by

$$\tilde{\theta}(k) = \begin{cases} 0 & \text{if } \hat{u}_1(k) = 1 \ \& \ \hat{u}_2(k) = 1 \\ \theta(k) & \text{if } \hat{u}_1(k) = 1 \ \& \ \hat{u}_2(k) = 0 \\ \tilde{\theta}(k-1) & \text{otherwise} \end{cases} \tag{23}$$

For the augmented state vector $\tilde{x}_f(k)$, the state equation is also augmented and with the above definition for $\tilde{\theta}(k)$ as,

$$\tilde{x}_f(k) = \tilde{F}(k)\tilde{x}_f(k-1) + \tilde{G}\varepsilon(k) \tag{24}$$

where $\tilde{F}(k)$ and $\tilde{G}$ are given as

$$\tilde{F}(k) = \begin{pmatrix} [1-\hat{u}_1(k)] & \hat{u}_1(k)[1-\hat{u}_2(k)] & \hat{u}_1(k)[1-\hat{u}_2(k)]T_s & \frac{1}{2}\hat{u}_1(k)[1-\hat{u}_2(k)]T_s^2 \\ 0 & [1-\hat{u}_2(k)] & [1-\hat{u}_2(k)]T_s & \frac{1}{2}[1-\hat{u}_2(k)]T_s^2 \\ 0 & 0 & 1 & T_s \\ 0 & 0 & 0 & 1 \end{pmatrix}, \quad \tilde{G} = \begin{pmatrix} \frac{1}{2}T_s^2 \\ \frac{1}{2}T_s^2 \\ T_s \\ 1 \end{pmatrix}. \tag{25}$$

With these representations, the Kalman filter is used to estimate the states.

Remark 4. *The measurement variance R of the noise $v(k)$ needs selection for filtering but it varies over time. We modify the real-time update of noise variance in [31] as follows:*

$$R(k) = \begin{cases} \frac{(\hat{\varepsilon}(k|k-1)T_s)^2}{12} & \text{if } y(k) \neq y(k-1) \\ R_w & \text{otherwise} \end{cases} \tag{26}$$

where R_w is a small positive constant.

4.4. Filtering results

The above formulation provides a representation of the data from the fibre optic sensor, and we can use the Kalman filter to estimate the state vector $\tilde{x}_f(k)$. It should be noted that, the reference measurement $y(k)$ is a piece-wise constant signal output which changes only at every $\Delta_\theta = 40°$, with the only information about the relative angle being available at these sampling instances when there is a reset to 0 in $y(k)$. The Kalman filter, however, can estimate the relative spindle angle $\theta(k)$ at each sampling instant by leveraging the model and the piece-wise constant signal $y(k)$, such that $\hat{\theta}(k) = [0 \quad 1 \quad 0 \quad 0]\hat{\tilde{x}}_f(k)$. For the example in-process data given in Figure 4a, its filtering results are shown in Figure 6. From Figure 6a, we can see that the spindle's relative angle can be estimated in real-time to obtain an accurate drilling interval for the spindle's initial degree of around 0°. The initial error is due to the mismatch between the spindle and estimator initial angles, which is eliminated at the first double notch signal.

Furthermore, the proposed framework offers an estimation of the spindle speed $\hat{\omega}(k) = [0 \quad 0 \quad 1 \quad 0]\hat{\tilde{x}}_f(k)$ (further multiplied by $60/360$ to transfer the unit from $degree/sec$ to RPM), which illustrated in Figure 6b. The estimated spindle speed fluctuates around the control command as given in Table 3 due to disturbances from the machining operation. The results confirm the effectiveness of the proposed signal processing framework for the fibre optic sensor in extracting the useful information about spindle speed and angle. Both of these offer useful information for the tool position and orientation that is useful for spatial localisation.

Remark 5. *For the spindle angle estimate, the steady-state envelope of the covariance was found to reach a maximum of about 9.4×10^{-7} rad^2, corresponding to a 1σ standard deviation of 0.00097 rad (approximately $0.056°$). This bound defines the steady-state uncertainty of the angle estimation and demonstrates that the estimator can reliably track spindle rotation with an accuracy better than $0.1°$.*

Remark 6. *Note that the rotational angle and speed estimation is normally carried out from an encoder sensor signal. However, due to machine warranty not being voided and the reliability issues of edge devices, as well as challenges with synchronisation to other sensor data, not to mention the slower acquisition rate, the raw encoder signal was not*

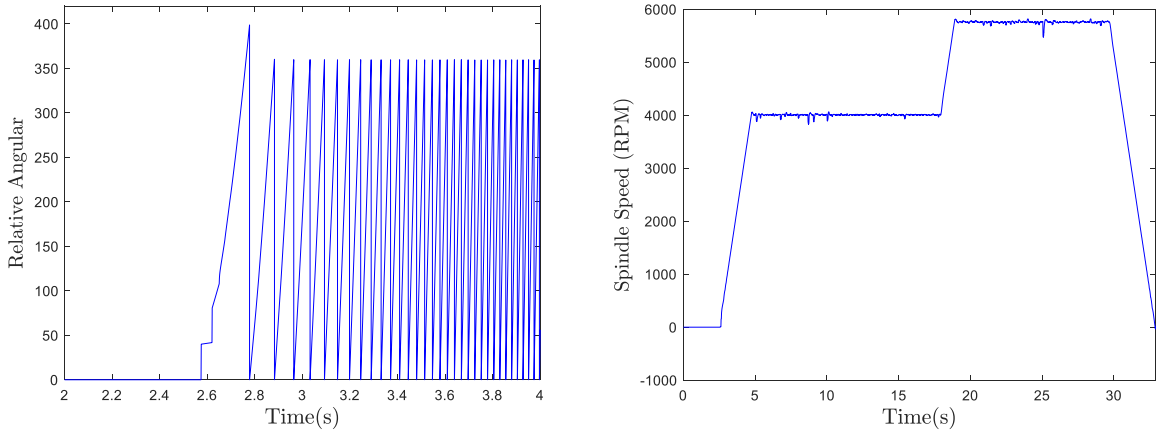

(a) The estimated relative angle $\theta(k)$ within [2s,4s].

(b) The estimated spindle speed $w(k)$.

Figure 6: Filtering results for fiber optic sensor.

utilised in this study. The fibre optic sensor solution has been shown to be generally useful in research environments as it is reasonably cheap and has flexibility in terms of its integration with other sensors. It also can be an option for retrofitting old machine tools that do not have encoders.

5. Visualisation and identification

5.1. Sensor signal integration framework for visualisation

The steps followed in the study can be described as follows:

1. Perform the drilling tests and use monitoring sensors to record the in-process data;
2. Design signal processing method (including filtering, amplification, modulation) for the acquired in-process data to enhance signal quality and extract useful information;
3. Use the real experiment data to create a visualisation for the machining process;
4. Separate the whole machining process into different segments based on the visualisation;

Step 1 is the basic step to obtain the in-process signal. Steps 2-4 establish a sensor signal integration framework that localises potential defects by linking them to specific spatial regions within the machining process. In this paper, we mainly focus on the design of the sensor signal integration framework and hence the process of performing Step 1 is skipped for brevity.

After obtaining the estimation of tool position as the z-axis displacement from the laser sensor and the relative angle of the spindle from the fibre optic sensor as in Sections 3 and 4, the tool can be localised to a specific depth and relative angle at any specific given time. This allows a visualisation for the drilling process in which other in-process data can be localised to a spatial region.

5.2. Visualisation of relative tool position with AE data

AE signals are a powerful tool to monitor the machining process. AE sensors can detect the transient elastic stress wave that is caused by material deformation [32]. In this article, we provide a visualisation with AE Data for analysis, noting that this method can be applied to other sensors (e.g., force and vibration sensor data) as well. For the example drilled hole, the available laser displacement signal is with a sampling rate of $25,600 Hz$ and the AE signal is sampled at $2,000,000 Hz$, which needs harmonisation. This requires a down-sampling of the AE data, having checked that there is no loss of information in this process. Here, the down-sampling is achieved by computing the root mean square (RMS) value of the AE signal within the intervals between two successive sampling points of the laser displacement signal measurement and replacing that interval with this RMS value.

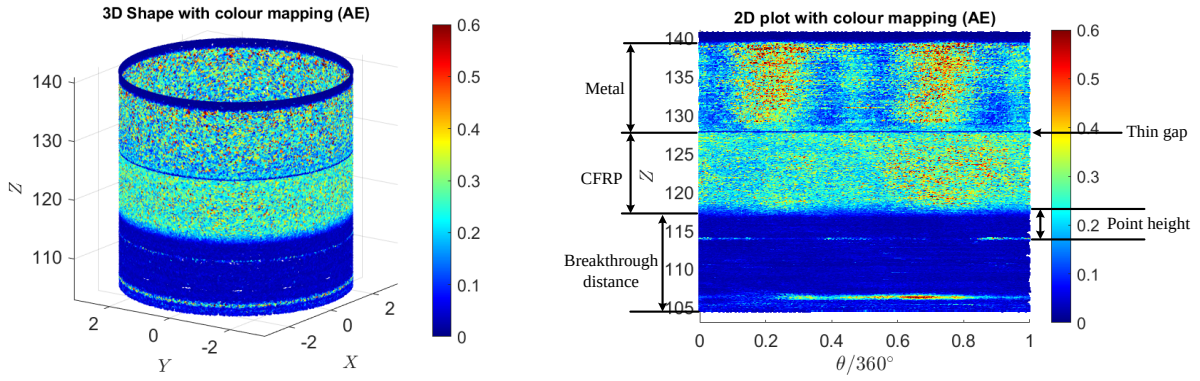

(a) 3D visualisation of the AE signal along relative tool position.

(b) 2D visualisation of the AE signal along relative tool position.

Figure 7: Visualisation of the sensor data during drilling process with relative tool position and angle. Colourmap indicates the RMS AE amplitude value. Magnitudes of X, Y and Z axes are in *mm* with $R = 3.175$ cutting radius in (a) while Y-axis in (b) is normalised angle $\theta/360 \in [0, 1]$.

Using the estimation of z-axis displacement (as in Figure 3a) and the relative angle (as illustrated in Figure 6a) and the RMS value of AE signal (recorded by the wideband differential AE sensor, and the signal is shown in Section II in the Supplementary Material), we can plot the drilling process's 3D and 2D visualisation in Figures 7a and 7b. The figure shows the tool tip position with relative height and angle as the hole is drilled with the AE RMS value as the tool machines the hole. Both figures show segmented patterns of drilling in different materials, useful for localisation of any defects, although it should be noted that the tool is represented as a single point for visualisation and is not reflective of the ground truth.

In Figure 2, there is delamination at the hole exit, as is often seen as a result of drills breaking through FRP surfaces (illustration of the breakthrough segment and point height are given in Section 3 in the Supplementary Material). Hence in the next section, we will segment the in-process data and only focus on the region when the tool is at the breakthrough segment.

5.3. Segmentation and defect spatial localisation

The analysis of potential features related to exit hole defects involves comparing signal features within the breakthrough segment to the observed defect. To allow comparison of signal features to hole quality images, we align all the breakthrough segment's in-process data together as in Figure 8a. Signals from the fibre optic sensor are utilized to estimate spindle speed and angular position. Simultaneously, signals from the laser displacement sensor are employed to estimate the feed rate and displacement. Sensed signals considered are the accelerometer readings, and AE signals. These are shown in Figure 8a where the time period associated with anomalous patterns in the sensor signals is highlighted in red. The maximum amplitude of vibration and the RMS profile of the AE signal, within this time interval, are much larger than the preceding and following time periods. These oscillatory signals can be further investigated through a 2D visualisation of the AE RMS signal. As seen in Figure 8b as a 'hot spot', this oscillatory time series is due to a defect associated with a particular relative angle and at a specific depth.

5.4. Comparison with a defect-free hole

To assess the ability of the proposed framework to detect defects, we apply it to a relatively defect-free hole (as shown in Figure 9a). Figure 9b shows the visualisation of the AE RMS signal with reference to relative tool position and angle for the breakthrough segment of this defect free hole. No hot spots are visible once the point height of the drill has completely cleared the bottom surface of the coupon. This is in contrast with the previous example with delamination and uncut fibres.

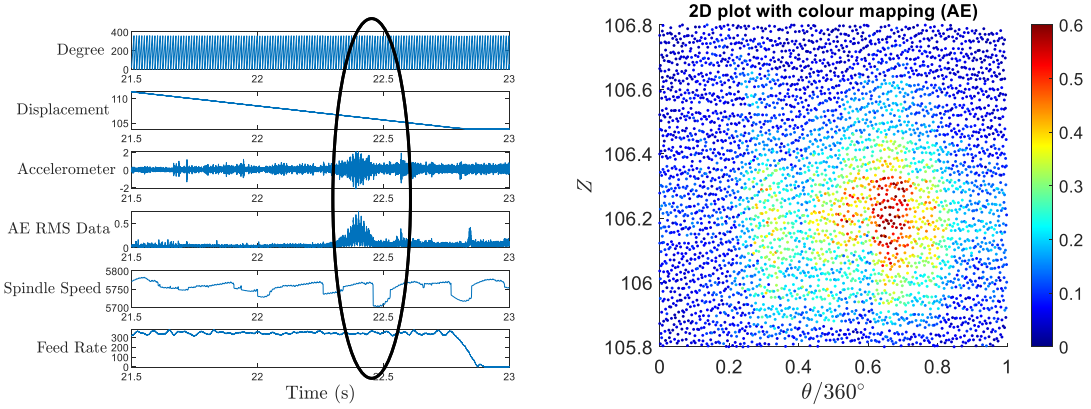

(a) In-process data in the breakthrough segment. (b) Anomalous signal pattern.

Figure 8: Localisation and defect identification in the breakthrough segment.

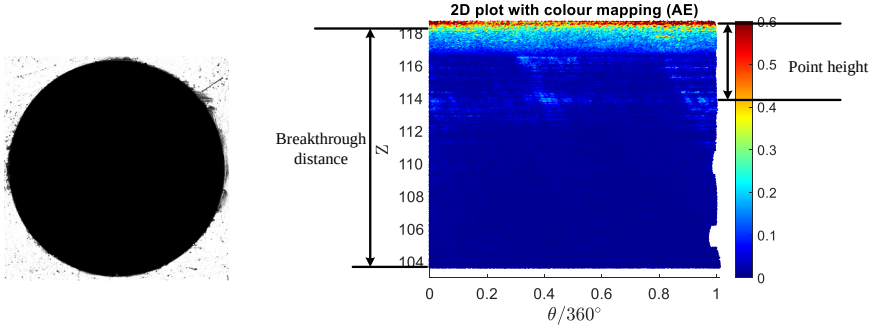

(a) Hole exit. (b) The signal pattern in the breakthrough segment.

Figure 9: Defect free hole and the signal 2D plot in the breakthrough segment.

6. Conclusion

This study has proposed a sensor signal integration framework to support spatial domain mapping by enabling the accurate estimation of tool position and orientation during the drilling of metal-composite stacks. This allows for localisation of in-process signals to specific spatial regions of the parts being machined and thus to facilitate defect localisation. It integrates multiple components: (i) a laser displacement sensor whose output signal is processed with a Kalman filter to enhance the accuracy of tool position and feed rate by processing displacement signals with noise; (ii) a fibre optic sensor used to estimate spindle speed and precise relative angular position of the tool by the characterisation of the sensor followed by the application of a Kalman filter based algorithm to process the sensors response to received light intensity; (iii) the amplitude of in-process data (e.g., AE signal, vibration) that is directly obtained from the sensors on the work-piece.

By integrating and visualising positional sensor data with in-process signals, this framework offers a promising approach for process monitoring and defect localisation. The framework was applied to holes with varying levels of defect at the exit. Pattern features could be seen in the AE data when plotted in the spatial domain. Plots showed bands approximately aligning with material layers and the gap between layers, as well as 'hot spots' of large AE signal amplitudes that have previously been known to be associated with defects. While these initial results demonstrate the potential of spatial signal mapping for revealing drilling anomalies, the current study does not yet provide a quantitative correlation between the spatial maps produced and the location/type of defects. This is primarily due to the variety of defects observed (e.g., burrs, delamination, uncut fibres), which were not separately labeled or isolated in the

present trial. Future work will involve controlled drilling experiments with higher sample sizes and detailed post-process inspection, aiming to build statistically meaningful links between signal features and distinct defect modes. In particular, quantitative image-based evaluation methods such as the pixel-based hole quality framework recently proposed in our conference paper [33] will be incorporated. This further investigation will enable the proposed spatial mapping framework to be cross-validated with established quality metrics such as the delamination factor F_d, thereby supporting its integration into predictive and real-time quality monitoring systems.

Acknowledgement

This work was supported by the UK Engineering and Physical Sciences Research Council (EPSRC) EP/P006930/1. The data used was generated in the UK Aerospace Technology Institute funded project "One-Way Assembly Sensor-based digital verification -Technology accelerator – Phase 1" IUK-113347. The trials and image capture were supported by AMRC members: Andrew Oakley, Oliver Hayes, Emma Warren, Yousef Bhaker, Michael Garrett, Sean Delaney, Luke Rutter, Lucy Mello and John Carmichael.

Declaration of competing interest

The authors declare that they have no known competing financial interests or personal relationships that could have appeared to influence the work reported in this paper.

Supplementary material

The supplementary material for this article is available in the submitted files.

CRediT authorship contribution statement

Bin Chen: Conceptualization, Methodology, Software, Validation, Formal analysis, Writing - Original draft preparation. **Chaoyue Niu:** Formal analysis, Software, Validation, Writing - review and editing. **Erica Smith:** Investigation (machining trials), Data Curation, Writing - review and editing. **Rob Bramley:** Investigation (machining trials), Data Curation, Writing - review and editing. **Pete Crawforth:** Resources, Supervision, Funding acquisition, Writing - review and editing. **Mahdi Mahfouf:** Supervision, Funding acquisition, Writing - review and editing. **Visakan Kadirkamanathan:** Conceptualization, Supervision, Project administration, Funding acquisition, Visualization, Writing - review and editing.

References

[1] A. P. Mouritz, Introduction to Aerospace Materials, Woodhead Publishing, 2012.
[2] S. Frutos-Taravillo, E. Paroissien, Y. Landon, S. Schwartz, M. Fressinet, C. Chirol, A review on metallic drilling burrs: Geometry, formation and effect on the mechanical strength of metallic assemblies, ASME Journal of Manufacturing Science and Engineering 147 (2024) 1–20.
[3] D. Geng, Y. Liu, Z. Shao, Z. Lu, J. Cai, X. Li, X. Jiang, D. Zhang, Delamination formation, evaluation and suppression during drilling of composite laminates: A review, Composite Structures 216 (2019) 168–186.
[4] J. E. Muelaner, A. Kayani, O. Martin, P. Maropoulos, Measurement assisted assembly and the roadmap to part-to-part assembly, in: 7th International Conference on Digital Enterprise Technology, 2011, pp. 11–19.
[5] C. Cooper, J. Zhang, Y. Guo, R. X. Gao, Surface roughness prediction through gan-synthesized power signal as a process signature, Journal of manufacturing systems 68 (2023) 660–669.
[6] S. Dong, W. Liao, K. Zheng, J. Liu, J. Feng, Investigation on exit burr in robotic rotary ultrasonic drilling of CFRP/Aluminum stacks, International Journal of Mechanical Sciences 151 (2019) 868–876.
[7] X. Rimpault, J.-F. Chatelain, J. E. Klemberg-Sapieha, M. Balazinski, Burr height monitoring while drilling CFRP/Titanium/Aluminium stacks, Mechanics & Industry 18 (2017) 1–11.
[8] M. O. Cole, P. Kuresangsai, P. Puangmali, T. Wongratanaphisan, C. Chamroon, A new active-thrust tool spindle and integrated force measurement technique for robotic drilling, IEEE/ASME Transactions on Mechatronics 30 (2024) 108–118.
[9] C. Li, Y. Lei, L. Guo, E. Zio, H. Gao, B. Yang, Gmm-binseg: a data segmentation method for cfrp/aluminum stacks drilling–countersinking monitoring signal, IEEE Transactions on Instrumentation and Measurement 73 (2024) 1–10.
[10] I. Urresti-Espilla, M. Telleria, I. Llanos, L. N. López de Lacalle, Cfrp drilling–induced defect investigation: part quality characterization and process monitoring approach, The International Journal of Advanced Manufacturing Technology (2025) 1–14.
[11] E. G. Plaza, P. N. López, E. B. González, Efficiency of vibration signal feature extraction for surface finish monitoring in cnc machining, Journal of Manufacturing Processes 44 (2019) 145–157.

[12] G. Rao, G. Wang, X. Yang, J. Xu, K. Chen, Normal direction measurement and optimization with a dense three-dimensional point cloud in robotic drilling, IEEE/ASME Transactions on Mechatronics 23 (2017) 986–996.
[13] X. Zhang, M. Li, D. Huang, Surface quality and burr characterization during drilling CFRP/Al stacks with acoustic emission monitoring, Journal of Manufacturing Processes 98 (2023) 138–148.
[14] M. Papananias, T. E. McLeay, M. Mahfouf, V. Kadirkamanathan, A bayesian information fusion approach for end product quality estimation using machine learning and on-machine probing, Journal of Manufacturing Processes 76 (2022) 475–485.
[15] M. Leco, T. McLeay, V. Kadirkamanathan, A two-step machining and active learning approach for right-first-time robotic countersinking through in-process error compensation and prediction of depth of cuts, Robotics and Computer-Integrated Manufacturing 77 (2022) 102345.
[16] A. Pardo, M. Majeed, R. Heinemann, Process signals characterisation to enable adaptive drilling of aerospace stacks, Procedia CIRP 88 (2020) 479–484.
[17] J. Zhang, R. Heinemann, O. j. Bakker, Process incidence monitoring in material identification during drilling stacked structures using support vector machine, The International Journal of Advanced Manufacturing Technology 136 (2025) 827–840.
[18] B. Denkena, M.-A. Dittrich, J. Mainka, Simulation-based feed rate adaptation considering tool wear condition, Procedia Manufacturing 52 (2020) 133–137.
[19] B. Denkena, E. Abele, C. Brecher, M.-A. Dittrich, S. Kara, M. Mori, Energy efficient machine tools, CIRP Annals 69 (2020) 646–667.
[20] B. Yang, F.-Z. Xuan, S. Chen, S. Zhou, Y. Gao, B. Xiao, Damage localization and identification in wgf/epoxy composite laminates by using lamb waves: Experiment and simulation, Composite Structures 165 (2017) 138–147.
[21] X. Liu, X. Zeng, Y. Yu, B. Zhao, Y. Wang, X. Qing, Localization and quantification of different types of defects in composite structures with smart sensor layers, Structural Control and Health Monitoring 29 (2022) e3043.
[22] Z. Zhou, Z. Cui, J. Liu, T. Kundu, A rapid technique for detecting and localizing damage in composite laminates, Engineering Fracture Mechanics 277 (2023) 108995.
[23] A. Graves, O. L. Blanch, D. S. Fernández, M. Jackson, In-process fingerprints of dissimilar titanium alloy diffusion bonded layers from hole drilling force data, Metals 12 (2022) 1353.
[24] B. Chen, C. Niu, E. Smith, R. Bramley, P. Crawforth, M. Mahfouf, V. Kadirkamanathan, A novel spindle speed and angle estimation strategy in multi-material robotic drilling, in: 2024 IEEE 20th International Conference on Automation Science and Engineering (CASE), IEEE, 2024, pp. 1222–1227.
[25] K. Zadafiya, D. Bandhu, S. Kumari, S. Chatterjee, K. Abhishek, Recent trends in drilling of carbon fiber reinforced polymers (cfrps): A state-of-the-art review, Journal of Manufacturing Processes 69 (2021) 47–68.
[26] L. Romoli, A. Lutey, Quality monitoring and control for drilling of cfrp laminates, Journal of Manufacturing Processes 40 (2019) 16–26.
[27] M. Li, M. Huang, Y. Chen, P. Gong, X. Yang, Effects of processing parameters on kerf characteristics and surface integrity following abrasive waterjet slotting of ti6al4v/cfrp stacks, Journal of Manufacturing Processes 42 (2019) 82–95.
[28] X. R. Li, V. P. Jilkov, Survey of maneuvering target tracking. Part I. Dynamic models, IEEE Transactions on Aerospace and Electronic Systems 39 (2003) 1333–1364.
[29] N. Kovvali, M. Banavar, A. Spanias, An introduction to Kalman Filtering with matlab examples, Springer Nature, 2022.
[30] M. Basseville, I. V. Nikiforov, Detection of abrupt changes: Theory and application, volume 104, Englewood Cliffs: Prentice Hall, 1993.
[31] T. Shi, Z. Wang, C. Xia, Speed measurement error suppression for PMSM control system using self-adaption Kalman observer, IEEE Transactions on Industrial Electronics 62 (2014) 2753–2763.
[32] M. Li, D. Huang, H. Han, X. Yang, Chatter detection and identification in high-efficient robotic milling CFRP composites using acoustic emission technique, International Journal of Precision Engineering and Manufacturing-Green Technology 10 (2023) 1155–1167.
[33] C. Niu, B. Chen, E. Smith, R. Bramley, P. Crawforth, M. Mahfouf, V. Kadirkamanathan, Pixel-based hole quality evaluation in robot drilling manufacturing process, in: 2024 IEEE 22nd International Conference on Industrial Informatics (INDIN), IEEE, 2024, pp. 1–6.